CrystEngComm

A Review on Synthesis and Engineering of Crystal Precursors Produced Via Coprecipitation for Multicomponent Lithium-Ion Battery Cathode Materials

Journal:	*CrystEngComm*
Manuscript ID	CE-HIG-05-2019-000679.R1
Article Type:	Highlight
Date Submitted by the Author:	18-Jun-2019
Complete List of Authors:	Dong, Hongxu; University of Virginia, Chemical Engineering Koenig, Gary; University of Virginia, Department of Chemical Engineering

Title: A Review on Synthesis and Engineering of Crystal Precursors Produced Via Coprecipitation for Multicomponent Lithium-Ion Battery Cathode Materials

Authors names and affiliations:

Hongxu Dong, Gary M. Koenig Jr.

Department of Chemical Engineering, University of Virginia, 102 Engineers Way, Charlottesville, VA, USA22904-4741.

Email address:

Hongxu Dong, hd5cw@virginia.edu;

Gary M. Koenig Jr., gary.koenig@virginia.edu.

Corresponding author:

Gary M. Koenig Jr

Department of Chemical Engineering, University of Virginia, 102 Engineers Way, Charlottesville, VA, USA22904-4741

1-434-982-2714 phone

1-434-982-2658 fax

gary.koenig@virginia.edu

Abstract

Interest in developing high performance lithium-ion rechargeable batteries has motivated research in precise control over the composition, phase, and morphology during materials synthesis of battery active material particles for decades. Coprecipitation, as one of the most reported methods in the literature to produce precursors for lithium-ion battery active materials, has drawn attention due to its simplicity, scalability, homogeneous mixing at the atomic scale, and tunability over particle morphology. This highlight summarizes the advancements that have been made in producing crystalline particles of tunable and complex morphologies via coprecipitation for use as lithium-ion battery precursor materials. Comparison among different crystallization reagents, solution conditions that influence the properties of crystal particles, and the fundamental knowledge from equilibrium and/or kinetic study of the coprecipitation processes, are systematically discussed. The research reports and guiding principles summarized in this highlight are meant to improve selections made by researchers to efficiently determine synthesis conditions. In addition, it is desired that the methods applied from the study of crystallization process will inspire researchers to pursue further investigation of the nucleation and growth mechanisms of these coprecipitation processes, which will be necessary to achieve truly predictive particle synthesis.

1. Introduction

Interest in developing high energy, high power, and safe electrochemical energy storage has motivated research in battery technologies for many decades [1–5]. Lithium-ion (Li-ion) rechargeable batteries, since their commercialization by Sony in the early 1990s, have received much attention over the last three decades due to the intrinsically high volumetric and gravimetric energy density and also excellent charge/discharge efficiency and cycle life [6]. While in most cases commercial cells use similar active material cell chemistry of a graphite anode and layered transition metal oxide cathode [7–10], many methods have been developed to synthesize these electroactive materials with the goal of control over the particle composition, morphology, and surface functionality [11–19]. The motivation to have exquisite control over active material composition and morphology is that the performance of the final assembled battery cell is highly sensitive to these parameters – both due to the properties of the individual particles themselves and to their organization within the electrode [17,20–24].

One of the methods very popular to produce Li-ion battery active materials is coprecipitation. Coprecipitation is commonly used due to its simplicity, scalability, homogeneous mixing at the atomic scale, and particle morphology control [25–27]. The process of using coprecipitation to synthesize battery active materials usually involves two main steps: first the formation of particles from a coprecipitation reaction which are normally referred to as precursors. The precursors are typically dried to remove residual water and/or other solvents. The precursor particles are then blended with a lithium source and calcined to produce the final active materials used in battery electrodes[28–32]. Due to homogeneous mixing at the atomic scale provided by the coprecipitation reaction, relatively mild calcination temperatures and holding times are needed to form the final product with its target phase and crystallinity [28]. These relatively mild calcination conditions are also beneficial for retaining the secondary morphology of the original precursor particles, although the surface roughness and/or primary particles that make up the secondary particles are

often modified due to decomposition of some of the precursor particle constituents and/or sintering [33]. The precursor decomposition also results in internal porosity, the structure and degree of which is highly sensitive to the precursor material chemistry and the calcination conditions [17,34,35]. Coprecipitation for production of battery materials is often conducted in batch processes in the literature, but the process has also been reported using continuous reactor systems which are highly scalable for mass production of battery active material powders [28,36]. There are many controllable parameters for coprecipitation synthesis that can significantly impact the composition and morphology of the particles including: temperature, pH, concentration of both species that participate in the coprecipitation reaction and their counter ions in solution, stirring rate and mixing within the reactor, mixing method, rate of reactant feed, and the use of additives that modify the particle morphology such as chelating agents [37–40]. The variety of coprecipitation chemistry and reaction conditions have resulted in many different particle morphologies including spheres, cubes, rods, plates, hollow spheres, dumbbells, rhomboids, and others [41–51]. A few examples of the diverse morphologies from literature reports are shown in Figure 1. Thus far, detailed knowledge of the fundamental processes that would enable rational and predictive control of final particle composition and morphology that includes solution chemistry, process variables, and particle nucleation and growth has been lacking, but efforts have been made to tackle some aspects towards achieving this outcome such as probing the impact of solution chemistry equilibrium on particle morphology or detailed process optimization reports [37–40,52,53].

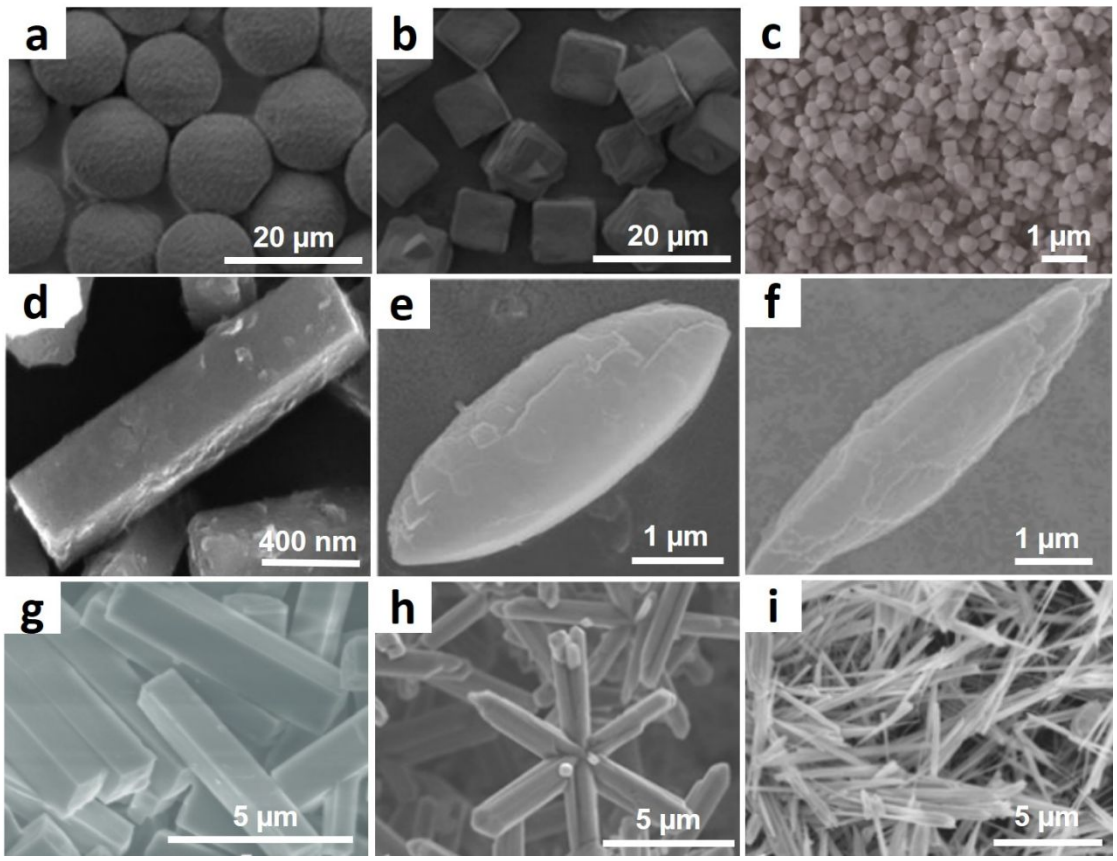

Figure 1. Particles with different morphologies obtained from coprecipitation reactions: a) spheres, b) cubes, c) cubes, d) rods, e) ellipsoids, f) elongated ellipsoids, g) rods, h) stars, and i) needles. a, b) Reprinted with permission from [51]. Copyright (2015) Elsevier. C) Reprinted with permission from [41]. Copyright (2014) Royal Society of Chemistry. d, e, f) Reprinted with permission from [44]. Copyright (2017) American Chemical Society. g) Reprinted with permission from [48]. Copyright (2016) Wiley. h, i) Reprinted with permission from [54]. Copyright (2006) American Chemical Society.

The study of coprecipitation broadly has a long history and the process has been developed for many applications including metal mining, water treatment, catalyst production, and pharmaceutical synthesis[55–58]. However, the use of coprecipitation as a popular method for the synthesis of Li-ion battery materials has been more recent and was spurred by commercialization of early Li-ion batteries. While solid-state and sol-gel synthesis were among the most popular for producing Li-ion active materials in the early literature and are still common today, coprecipitation has grown in popularity over the last 15-20 years. Evidence of this growth can be found using a Web of Science™ topical search including “precipitation”, “lithium”, and “battery” which in February 2019 found 921 publications, with 5 or less from 1995-2001 and

rising to the highest value of 123 in the most recent full year of 2018. This review will introduce a brief overview of some of the earliest coprecipitation papers in the Li-ion battery literature in Section 2, which often promoted the advantages of coprecipitation compared to more common synthesis methods such as solid-state and spray pyrolysis. In Section 3, the three most common types of coprecipitation in the Li-ion battery field will be discussed and compared: hydroxide, carbonate, and oxalate. The disadvantages and major concerns when using coprecipitation to synthesize materials will also be described. In Section 4, work will be summarized which has been reported to tune or control the particle morphologies by controlling the coprecipitation reactor conditions. This section will include possible relationships between reaction conditions and the final particle products, which is meant to provide an initial guide for researchers to consider for producing final particle products with desired properties (e.g., composition and morphology). In Section 5, equilibrium and kinetic studies will be summarized which have explored coprecipitation reactions both in batch and continuous systems. In the final section, more complex materials produced via coprecipitation will be described such as compositional core-shell structures and concentration gradient materials.

2. Development and Expansion of Coprecipitation for Li-Ion Battery Active Materials

Solid-state synthesis routes are among the oldest and most common methods reported in the literature for making battery active materials [59–63]. A major advantage is the ease in achieving the correct stoichiometry of transition metal (TM) and Li through careful measurement of the constituent powders – although depending on the processing and particle size long hold times at elevated temperatures may be needed [60,64–66]. The use of solid-state reaction to synthesize intercalated TM oxide as cathode materials in rechargeable Li-ion batteries dates back to at least the 1980s and all the most well-known cathode materials including layered phase $LiCoO_2$, spinel phase $LiMn_2O_4$, and olivine phase $LiFePO_4$ were first synthesized by using solid-state reactions [67–70]. More specifically, Mizushima et al. used a high temperature solid-state

method to synthesize $LixCoO_2$ cathode materials [67]; Thackeray et al. used solid-state method to synthesize lithiated manganese spinel and measured the electrochemical properties as battery cathode [69]; solid-state was also used to synthesize phosphor-olivines for rechargeable lithium batteries first by Padhi et al. [68]; and Guyomard and Tarascon utilized solid-state reaction to synthesize $Li_xMn_2O_4$ powders in their review paper[71]. Relatively high temperature and long firing time are typically necessary in solid-state synthesis. As was described in papers from Gummow et al. [9,72], $LiCoO_2$ prepared at low temperature exhibited disordered cation distributions, and such disorder also occurred in $LiCo_{1-x}Ni_xO_2$ for the range $0 < x \leq 0.2$. When $x > 0.2$ severe phase impurities were detected. In addition to the long firing time at high temperatures, which has high energy demands, sometimes high pressure, aggressive milling, and pellet making have also been employed to guarantee high phase purity [7,73–76]. Solid-state synthesis has TM and Li constituents that must move relatively large distances through solid phases to find their desired atomic positions, and thus high temperature and intimate contact helps to accelerate the diffusion process and long firing times aid in allowing the solid structure to approach equilibrium. An additional complication can be that different preparation conditions such as firing temperature and cooling rates can play a role in oxygen loss or uptake in the final materials, either of which impacts phase purity [77–81]. Loss of Li from the material with extended firing times at elevated temperature can also impact the resulting phase and/or electrochemical performance of the active material [82,83]. Another challenge of aggressive firing conditions is that the materials may be metastable, resulting in changes to the oxidation state of different elements and even the phase due to oxygen lose and high temperature conditions, especially for nickel containing TM oxides [10,84]. An alternative is to fire the materials under relatively low temperatures (400-600°C) for much longer times approaching a few days [85,86], although such processes are still energy and time intensive.

To synthesize phase pure TM oxides that have structural sensitivity to long/high temperature firing, researchers started to report the use of 'precursor' methods for Li-ion battery materials to facilitate cation mixing and homogeneity. In Ohzuku's

work in synthesizing cobalt nickel oxide [7], known amounts of $Ni(NO_3)_2$ and $Co(NO_3)_2$ were dissolved in distilled water and LiOH solution was added to the solution heated at 60°C. The final materials were obtained by the thermal decomposition of the dried precursor at 800°C for 12h in air. Ni-rich $LiCo_{1-x}Ni_xO_2$ for the range $0.5 \leq x \leq 1$ was successfully obtained from this method, with the intimate mixing of the Co and Ni facilitated by their being dried from a solution where they were solvated and atomically distributed/mixed. Zhecheva et al. also implemented 'solution mixing' of multiple TM ions to synthesize oxide materials of targeted compositions [87], which was also used in Gummow's early synthesis work[9]. Solid Li_2CO_3 was added to a solution containing $Ni(NO_3)_2$ and $Co(NO_3)_2$ under intensive stirring. The mixture was evaporated to obtain a dry residue consisting of $LiNO_3$ and nickel and cobalt hydroxide nitrate, which was then pressed into pellets, calcined at 600°C for 6 hours in air, and then ground and pelletized again and calcined for 30 hours. The process was similar to conventional ceramic or solid-state synthesis route, but the 'wet chemistry' step was employed as a tool to facilitate better mixing between Li and the TMs. This method was followed by some later research for the synthesis of different Lithium TM oxides[88]. These solid-state routes where Li and TM salts or oxides are mixed (physical mixing or solution mixing), dried, pelleted, and fired under high temperature (and in some cases refired) are still common and reliable methods to produce battery active materials [89,90]. Besides the added time and complexity of repeated energy-demanding calcination firings, a major tradeoff with these methods is that morphology control or tunability is often challenging.

Spray pyrolysis is similar to the 'wet mixing' approach in that it also uses solution phase(s) to promote homogeneous cation mixing. Droplets are produced by nebulizers from pre-mixed solutions, and are further sent to high temperature furnaces where a series of physical and chemical processes including solvent vaporization, precipitation, and decomposition, will take place to produce the target materials [31,91,92]. Post-annealing improves the phase purity and can be used to modulate particle morphology. Zhu et al. published a detailed review on the use of spray pyrolysis method to synthesize battery active materials [93]. Spray pyrolysis

routes are commonly used to produce commercial TM oxide materials at large scale (yield capability can achieve up to tons per day) [93], while it is less common in academic research labs because of the increased equipment cost and complexity. A great number of factors will influence the properties of the final powders collected, such as solution concentration, nebulizer type and droplet sizes, and furnace temperature and residence time. While producing spherical particles via spray pyrolysis is common, producing other morphologies and complex compositional profiles is challenging. In addition, size distributions are often rather polydisperse, though the size and size distribution does have tunability and relation with the initial droplet distribution [93].

Following Ohzuku et al.'s report [7], Caurant et al. published an early report on the hydroxide coprecipitation method to synthesize battery cathode precursors [94]. Rather than using the conventional ceramic processes with multiple successive mixing, pressing, heating, and grinding stages of the powders, hydroxide coprecipitation was implemented in aqueous solutions to reduce material preparation time and effort while still aiming to achieve intimate homogeneous mixing between the multi-component TM ions. To synthesize $LiNi_xCo_{1-x}O_2$ materials, a solution with varying concentrations of LiOH and NH_4OH was added into a solution of $Ni(NO_3)_2$ and $Co(NO_3)_2$ in ratios of predefined stoichiometry. The multi-component hydroxide precipitates were obtained after a rotary evaporation process at 70°C under vacuum to remove residual water and ammonia. The products were then dried and calcined under a flow of oxygen, which was expected to decompose any last remaining ammonium nitrate. Ammonium was chosen in part to facilitate the hydroxide coprecipitation because it readily decomposed under mild thermal treatment and was thus not expected to impact the final material properties as an impurity. The same target oxide materials were also prepared for comparison via direct solid-state reaction of Li_2CO_3, NiO, and $CoCO_3$, in predefined stoichiometric proportions. Relative to the products synthesized through coprecipitation, the materials from the solid-state method exhibited poorer crystallinity and phase purity, and thus worse electrochemical performances, including lower capacities and larger

cell polarizations, even though longer calcination time was applied during the solid-state reaction as needed to form the target material. This study indicated improvements to mixing homogeneity when using coprecipitation relative to solid-state methods in achieving better cation mixing and phase purity in the final materials.

Spahr et al. published a report employing hydroxide coprecipitation in an oxidative environment to synthesize Mn substituted $LiNiO_2$ [95]. A hydroxide precipitate was filtered, washed, and then mixed with a 1.1-fold excess of Li in a LiOH solution. The mixture was dried and then calcined. Pure, single-phase oxide products were obtained with one step calcination, although there was deficiency found in the amount of Mn which was attributed to overoxidation of Mn and the formation of soluble MnO_4^- species. The materials obtained from coprecipitation were determined to have homogeneous ion mixing while avoiding the typical grinding, pressing, and heating cycles of solid-state methods. Note that the coprecipitation was intentionally conducted in a strongly oxidative environment which readily oxidized Mn from 2+ to 4+ and the transformation in oxidation state and phase of the precursor could impact final material homogeneity.

Paulsen et al. explored different synthesis routes based on the 'hydroxide mixing' method. In a study published in 2000 towards synthesis of $Li_{2/3}[Ni_{1/3}Mn_{2/3}]O_2$ materials, 'hydroxide mixing' was implemented as the first step to obtain a TM precursor [96]. A solution of TM nitrates was slowly dripped into a NaOH solution with intensive stirring. The obtained mixed hydroxide was filtered, washed, and calcined at 200°C for 2 days in air. The mixed oxide/hydroxide was then ground with excess Na_2CO_3, pressed into pellets, and a single calcination was made for 14 h at 900 °C (or 36 h at 700 °C) in air. This Na-containing TM oxide was then converted to Li TM oxide by ion exchange of Na for Li in molten salt. Compared with the previous 'hydroxide mixing' reports [94], this report separated and harvested the precipitates via filtering rather than evaporating the solution, which significantly reduced the time and energy associated with evaporative solvent removal. The formation of the Na TM oxide and

ion exchange of the material added extra steps and complexity relative to direct firing with a Li source but was utilized in their process to stabilize the structure of the target oxide materials. The same method was later applied to synthesize a variety of multicomponent Li TM oxide materials of composition $Li_{2/3}[Co_xNi_{1/3-x}Mn_{2/3}]O_2$ [97]. Shortly thereafter, minor modifications to the synthesis were reported where LiOH was directly mixed with the TM hydroxide precursors before the calcination to form the final cathode materials [98], reducing the number of process steps. More papers reported the same method around the same time and the blending of multicomponent TM hydroxide with Li salt followed by a single calcination has become a common route to producing Li-ion electrode active materials of targeted compositions [99–101]. While generally only a single firing step is used to convert coprecipitation precursors to final materials, the firing conditions to achieve complete crystallization of the product depends significantly on the homogeneity of the precursor and the chemistry of the precursor, and the target phase of the final materials can vary greatly [53,95]. It should be noted though that while coprecipitation has been often described and assumed to produce homogenous mixing at the atomic scale, proof of this level of mixing and the extent of its uniformity throughout the precursor particle population has not been demonstrated; to the contrary some reports have suggested more granular mixing scales likely exist within the precursor particle populations [66,94]. Even mixing at larger than atomic scales within coprecipitated particles will generally be a significantly smaller length scale than the commonly micrometers length scales encountered with particles in direct solid-state reaction of multiple powders.

There are many details in the firing of precursors that can significantly impact the resulting phase and morphology of the final materials. The precursors undergo a number of chemical and physical changes during processing and calcination, including decomposition of the precursor and formation of one or more oxide phase, the formation of solid solutions, and sintering. The composition and microstructure that may be desired can greatly vary depending on the specific material and target material/application. Calcination processes at elevated temperatures and hold times generally coarsen and sinter the primary particles that form after precursor

decomposition resulting in larger, smoother and flatter particle surfaces [30]. The changes in particle microstructure with extended firing time or elevated temperature also alters the internal porosity and can significantly impact the electrochemical performance of the active materials [33,102]. For instance, it was reported that layered transition metal oxide cathode materials have an optimal calcination temperature which resulted in relatively higher discharge capacity, rate capability, and cycle stability [33]; the higher discharge capacity and better rate capability were explained by larger exposed surface area provided by relatively smaller primary particles, which grew larger under higher calcination temperatures, while too low of the calcination temperature was not enough to create oxide final materials of appropriate phase purity and crystallinity. The slightly better cycling stability of oxide materials from lower temperature calcination, however, was not correlated with any synthesis condition or physical property in the paper; it may still be attributed to the smaller primary particle size which was found to be able to better accommodate internal stress during charge and discharge cycles without any mechanical deformation, compared to larger particles which exhibited fractures after the same number of cycles [103]. The details of calcination and post-processing of the final materials obtained from the coprecipitation precursors is important but outside of the scope of this review. Also, accurate in-situ tools to observe the change of microstructure of cathode materials during battery cycling need to be improved to more explicitly correlate the microstructure of active materials to their electrochemical performances [104]. In general, the porous microscale secondary particles formed from coprecipitation, composed of nanoscale primary particles formed after decomposition and sintering, are believed to be beneficial for the optimization of electrochemical properties, since the primary particles as well as the internal porous network means short Li-ion transportation distance and good electrolyte accessibility while the microscale secondary particle increases the tap-density and thus the energy density of the materials [105–109].This review will focus on the coprecipitation reaction and properties of the resulting precursors, including the phase purity of the precipitate crystal particles that are crucial to the properties of the final material product. An important aspect of the coprecipitated precursor

frequently retained in the final active materials, the particle morphology, will be discussed in detail in Section 4 along with the observations of how solution conditions direct particle morphologies. The tunability of particle morphologies from coprecipitation is a major advantage of the method. Details of common coprecipitation systems used to produce battery active material particles follow in the next section.

3. Coprecipitation of Transition Metals with Different Anions

Hydroxide coprecipitation was the earliest developed coprecipitation method used for TM oxide battery materials synthesis [94,96–98]. Chelating agents, such as ammonia and ammonium salts, were generally used to assist the production of dense spherical particles [110]. Hydroxide precipitates were reported with homogeneous cation mixing and monodispersity with regards to particle shape and particle size distribution [28,32,52]. Detailed discussion of particle morphology control through reaction conditions using coprecipitation will be covered in Section 4. Hydroxide coprecipitation does have some challenges: 1) Mn^{2+} will be oxidized to Mn^{3+} and Mn^{4+} in the presence of oxygen in air, forming MnOOH and MnO_2 impurities; 2) to prevent the formation of oxidized Mn impurity phases, the coprecipitation must be carried out in an inert atmosphere which adds complexity to the process; and 3) reproducibility of particle morphologies can be low due to the sensitivity of the particle nucleation and growth process to the solution conditions.

In 2002 Lee et al. published one of the earliest reports using carbonate coprecipitation to synthesize battery precursor particles [112]. The carbonate precursor was used to synthesize the high voltage spinel structure cathode material $LiMn_{1.5}Ni_{0.5}O_4$ (LMNO). In the synthesis, an ammonium carbonate solution and a TM solution containing appropriate stoichiometric feed amounts of Mn and Ni (3:1 Mn:Ni) dissolved from sulfate salts were poured into a batch reactor. Compared to the materials produced from a sol-gel process, no impurity phase was detected in the materials synthesized from the carbonate precursors. This was attributed to the

homogeneous mixing between the TM ions from the coprecipitation process, whereas in the sol-gel process isolated Ni failed to substitute into the Li Mn spinel phase. Scanning electron microscope (SEM) images showed the particles from coprecipitation were irregular secondary particles (3-4 um) composed of nano-sized primary particles (50-100 nm). In a follow up report， carbonate coprecipitation was applied to synthesize precursors used to make multi-component layered materials [13]. In these initial reports utilizing carbonate coprecipitations, particle size and shape control was not well defined. Also, in some cases the secondary particle aggregates would undergo significant fracture and break up of primary particles after the carbonate decomposition during calcination processes. In later works relatively uniform particle shape was obtained with narrower size distribution [33,113]; however, process variables that resulted in the more monodisperse particle morphologies were still under exploration. These early reports showed the possibility of particle morphology tuning by controlling the solution conditions from carbonate coprecipitation. And even though many of the precipitate particles had a relatively wide size distribution with irregular shapes, the aggregates became more uniform in shape and more densely packed with the aid of chelating agents [114,115]. The micrometers-sized secondary particles comprised of hundreds of nanometers-sized primary particles as the final product exhibited structural stability and highly accessible surface area as cathode materials, resulting in encouraging electrochemical performance and rate capability [28,53,91,116].

Carbonate coprecipitation has the following advantages: 1) almost all the commonly used TM cations for Li-ion batteries remain in the divalent oxidation state in carbonate coprecipitation solution within typical pH operating ranges; thus inert gas is not needed to assure phase purity of the product [33]; 2) the solution conditions of carbonate coprecipitation are relatively neutral with regards to pH. Later studies of carbonate coprecipitation have also mentioned some drawbacks of carbonate coprecipitation: 1) continuous growth of secondary particle sizes [117] in a continuous stirred tank reactor (CSTR) makes control of particle size monodispersity

challenging; 2) the large particle size and large surface area makes the precursor samples vulnerable to moisture [118]; 3) composition deviation from the feed or designed ratio due to the different solubilities of the precipitates [22]. For example, the relatively stronger coordination of ammonia with nickel ions cause Ni-deficit in the coprecipitate crystals when using ammonia as chelating agent [83]. 4) At high Ni compositions Ni impurity phases form [119]; 5) The larger carbonate constituent compared to hydroxide results in increased porosity on calcination to final active material. While this improves electrolyte accessibility to the particle interior which has advantages with regards to rate capability, the particle porosity makes the materials more susceptible to fracture during calendaring which is an important step in commercial electrode processing [117,120].

Oxalate has also been investigated as a coprecipitation agent with TM cations to produce battery precursors. In 2010 Park et al used oxalate coprecipitation to synthesize precursors for making multi-component olivine materials [31]. In this work the effect of the pH, atmosphere, temperature, and aging time was investigated with respect to the impacts on the atomic ratio of TMs, phase purity, and morphology of the mixed TM oxalate. Significant Mn-deficiency was observed due to the relatively higher solubility of Mn oxalate, when oxalic acid and TM sulfate salts were used to produce the precursors; improvement in obtaining the target stoichiometry was achieved by using ammonium oxalate as the oxalate source, which increased the solution pH. For Co and Fe, the oxalate β-phase was found to be preferred during room temperature coprecipitation and α-phase oxalate was observed during high temperature coprecipitation (90°C); in contrast Mn only exhibited α-phase oxalate for all conditions. To produce a phase pure precursor with homogeneous mixing of multiple TM cations, temperature was maintained at 90°C in the binary system to avoid formation of Mn-rich α-oxalate and Mn-lean β-oxalate. Optimized samples from oxalate coprecipitation exhibited significant improvements in rate capability, which confirmed the importance of phase and compositional homogeneity of the precursors for extracting the best electrochemical performance from the multi-component cathode materials. SEM images of final olivine samples from the ammonium oxalate

system showed nano-size crystals aggregated into irregular secondary structures. Mn-deficiency of the precipitate samples, especially at low pH conditions, was also studied by Wang et al. in 2013 [121]. They also reported that by using ammonium hydroxide as a pH adjuster and shifting the pH to near 7 the Mn to Ni ratio in the particles was much closer to the feed ratio in the synthesis of Li-rich Mn-rich layered cathode precursors. The final oxide particles were hierarchical structures with pores of regular patterns forming from aligned rod-like primary particles; the rod-cluster structure showed superiority over individual nano-sized primary particles produced after ball milling treatment with regards to both cycle life and rate capability.

In 2010 Wu et al published on the use of oxalate coprecipitation to synthesize precursors for $xLi[Li_{1/3}Mn_{2/3}]O_2.(1 - x)LiNi_{1/2}Mn_{1/2}O_2$ [122]. The obtained particles showed irregular shapes, similar to sol-gel materials. In 2013 Zhu et al. developed an oxalate-carbonate composite coprecipitation to synthesize precursors for the production of LMNO [83]. The stronger coordination of ammonia with Ni ions was known to result in Ni-deficit in the carbonate precipitate materials. Since both Ni and Mn oxalates have very little solubility in aqueous solution, ammonia had no significant effect in the equilibrium solution concentration of either TM cations, and experimental results showed that with ammonium oxalate as the precipitation reagent the obtained precipitate samples had stoichiometry almost identical to the feed. However, without the chelating agent dissolving/recrystallizing the particles, the obtained particles from pure oxalate precipitation were non-spherical; spherical and stoichiometric particles were obtained by adding small amounts of ammonium carbonate to oxalate coprecipitation.

Oxalate coprecipitation has a few advantages over hydroxide and carbonate coprecipitation: 1) oxalate ions in the solution play a dual role as both a precipitation agent and a complexing agent - the formation of metal complexes slows down the precipitation rate and makes the nucleation and growth of the particles more controllable [83]; 2) most TMs used in cathode materials, including Ni, Co, Mn, and their blends, form stable oxalate dihydrates across the entire range of mixing ratios [63,121],

which results in high purity precursors with homogeneous mixing across a wide range of compositional space. It is important to be aware that although the TMs all form oxalate dihydrates, different crystallographic structures may form under different temperatures and pressures [123–125]. Proper solution conditions must be chosen to prevent polymorph phase separation [18,121]. Oxalate precipitation also has some challenges. 1) Compositional deviations can occur between the precursor and the initial solution feed composition. Composition deviation from the feed also occurs for hydroxide and carbonate coprecipitation [28]; however, hydroxide and carbonate typically operate at higher total concentrations and higher precipitate yields, which mitigates the compositional deviation to the extent that it is often ignored in those systems. Compositional deviation from the feed can be significant when the reaction is conducted in low concentration regimes where slow precipitation rate is desired to control and tune precipitate growth and morphology [22,51]. Tuning the solution feeding ratio to target the final desired composition in the precursor has been used to improve material purity and electrochemical performance [22]. 2) Oxalate salts have relatively low solubility in aqueous solution, which limits the utility of chelation agents as particle morphology modifiers to make spherical particles [83]. Other chelating agents other than ammonia may be found which improve the particle morphology [126]; 3) oxalate salts and oxalic acid have relatively lower solubilities than hydroxide and carbonate species, which may limit the precipitate yield and production rates. 4) While many TMs are stable for oxalate coprecipitation in air, others require an inert atmosphere – in particular Fe^{2+} ions were reported to readily be oxidize to Fe^{3+} and result in iron deficiency for oxalate coprecipitation with this TM in air [31].

4. Operating Conditions and Influence on Particle Properties

Particles of a variety of different morphologies have been synthesized via coprecipitation, including spheres, rods, and plates as shown in Figure 1 [41–51,54]. Spherical particles are preferred in a number of cases, as spheres tend to pack relatively densely compared to irregular particles which leads to high tap density and

electrode loading, and also irregular particle shape can influence powder fluidity during processing, transfer, and mixing [127]. High tap density and electrode loading are desirable due to their correlation with energy density at the cell level [128,129]. Anisotropic particles can have advantages in certain cases though, for example in providing a shorter pathway for Li^+ diffusion out of the particle or in facilitating alignment of the active material particles within the electrodes for aligned pore microstructures to reduce electrode ion transport resistance [130]. This section will focus on reports of the influence of solution conditions on the particle morphology of the precursors and some of the particle morphologies obtained.

4.1. Transition metal salt anion effects

In a work published in 2003 by Jouanneau et al. the effects of using sulfate versus nitrate salts in hydroxide coprecipitation were studied with relation to the impact on particle tap density [53]. It was observed that for equivalent solution composition and processing conditions of particles, the precursors synthesized using TM sulfates had higher tap density for the final oxide materials relative to those using TM nitrate salts. The reason for the increase in tap density was not provided in the work. The morphology of the final oxide particles was also observed using SEM and the particles synthesized from TM sulfates consisted of large agglomerates (between 10 and 20 μm) of very small particles (around 0.2 μm), a structure which also resembled the morphology previously observed for particles from hydroxide coprecipitation using nitrates [27]. The existence of Li_2SO_4 impurities were identified in the final oxide sample of materials resulting from coprecipitation of TM sulfates; however, this impurity was eliminated by implementing pH control during the reaction and holding the pH at 14 by continuously adding LiOH to the solution.

Many of the hydroxide coprecipitation reports in the literature use TM sulfate source salts, likely in part due to the previous studies demonstrating high tap density using these TM salts and their widespread availability from chemical distributors. For example, a detailed study on the structure, and thermal stability of $Ni_xCo_{1-2x}Mn_x(OH)_2$ ($0 \leq x \leq 1/2$) particles was reported shortly after the report mentioned in the

preceding paragraph [131]. Kim et al. also adapted hydroxide synthesis from TM sulfates as precursors for $Li[Ni_{1/3}Co_{1/3}Mn_{(1/3-x)}Mg_x]O_{2-y}F_y$ materials [132]. Many reports in the literature of battery hydroxide precursors from TM sulfate salts can be found [52,53,92].

4.2. Chelating agent and stirring rate

Samsung SDI Co. published one of the earlier studies of the impact of ammonia as a chelating agent in hydroxide coprecipitation [110]. The report took advantage of ammonia to control the precipitate particle growth, and a patent was also filed on this process [110,133]. The function of ammonia was explained using the following reaction sequence (rearranged to a general form, M represents all possible transition metal ions):

$$M^{2+} + xNH_4OH(aq) \rightarrow M(NH_3)_n^{2+}(aq) + xH_2O \quad (1)$$

$$M(NH_3)_n^{2+}(aq) + yOH^- = M(OH)_2(s) + nNH_3 \quad (2)$$

In the proposed mechanism, ammonia forms complexes with TM ions in the solution, which then gradually react with hydroxide ions to form precipitates.

In the report, the pH was controlled and maintained by adding NaOH throughout the process. The obtained particles were sphere-like secondary particles composed of primary particles of sub-micron size, and the particle size of the secondary particles ranged from diameters of 5 - 30 μm in a typical population. The next year Ying et al. published a work on 'controlled crystallization' also using ammonia as the chelating agent in hydroxide coprecipitation to synthesize Co and Ni hydroxide particles [127]. The paper reported that with the aid of ammonia it was possible to increase the tap density of cathode materials without sacrificing the specific capacity by controlling particle morphology and size distribution. The obtained regular spherical hydroxide particles and final oxide particles were synthesized by using the chelating agent and the effect of ammonia concentration on particle morphologies was investigated. It was found that the particles became more spherical and had a narrower size distribution, which gave higher tap density, when higher concentrations of ammonia

were used. The optimized particles (pH 11.5, 0.6 M NH_3, having particle size 5-15 um), after conversion to layered oxide active material, surpassed the tap density and specific capacity of commercial reference materials when compared in battery cells. A later work published by Lee et al. in 2004 also reported the most regular spherical particles with the narrowest size distribution resulted when the highest amount of ammonia, the lowest pH, and the highest stirring speed was used within their investigation ranges (with the ranges being 0.12-0.36 M ammonia, pH 11-12, and stir rate of 400-1000 rpm) [82]. Figure 2 shows the evolution of particle morphologies as a function of ammonia concentration. Spherical particles with narrower size distribution were obtained from coprecipitation with higher ammonia amount, which also resulted in corresponding final materials with the highest tap density. Stirring speed was also found to play an important role in determining the secondary particle morphology in the coprecipitation. As shown in Figure 3, more spherical secondary particles composed of more densely packed primary particles formed as the stirring speed was increased from 400 to 1000 rpm from coprecipitation synthesis.

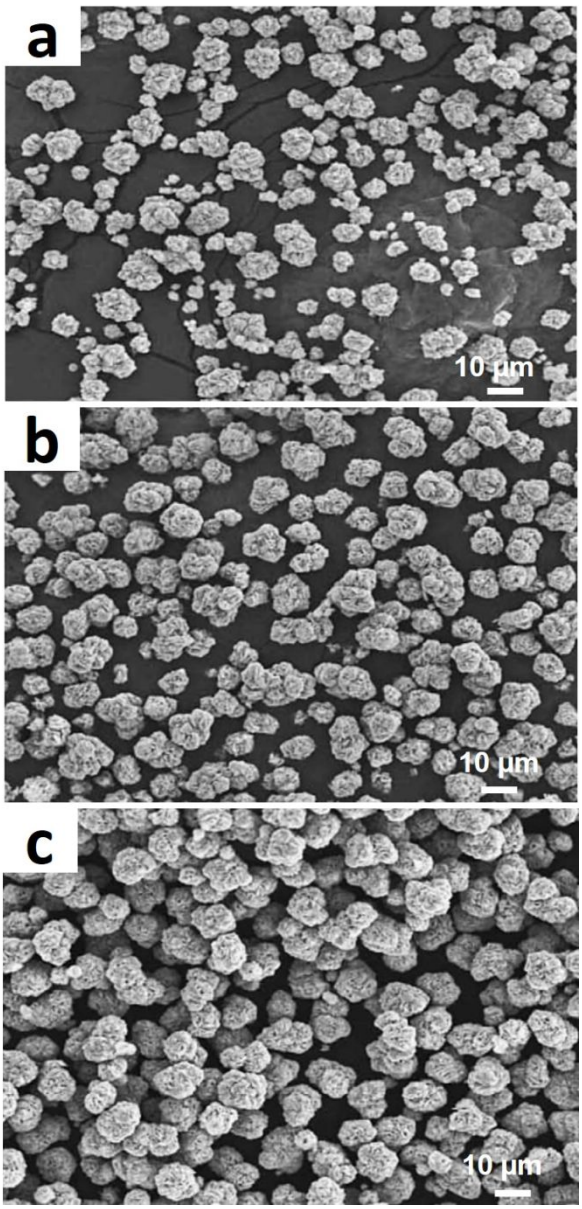

Figure 2 SEM images of $(Ni_{1/3}Co_{1/3}Mn_{1/3})(OH)_2$ powders produced from hydroxide coprecipitations at various concentrations of NH_4OH as a chelating agent. A) 0.12 mol dm^{-3} NH_4OH, b) 0.24 mol dm^{-3} NH_4OH, and c) 0.36 mol dm^{-3} NH_4OH while all the other solution conditions were controlled to be the same with total TM concentration and NaOH concentration both of 2.0 mol dm^{-3}, pH of 11, stirring rate of 600 rpm in a CSTR system. Reprinted with permission from [82]. Copyright (2004) Elsevier.

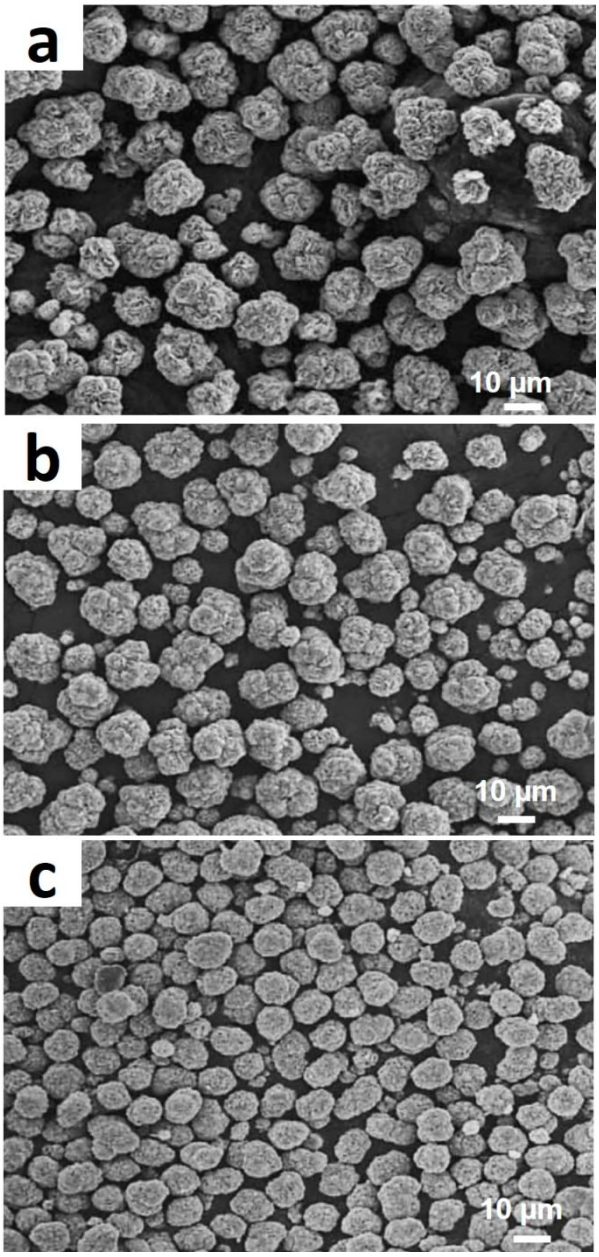

Figure 3 SEM images of $(Ni_{1/3}Co_{1/3}Mn_{1/3})(OH)_2$ powders produced from hydroxide coprecipitations at various stirring speeds. A) 400 rpm, b) 800 rpm, and c) 1000 rpm while all the other solution conditions were controlled to be the same with total TM concentration and NaOH concentration both of 2.0 mol dm^{-3}, pH of 11, and 0.36 mol dm^{-3} NH_4OH in a CSTR system. Reprinted with permission from [82]. Copyright (2004) Elsevier.

Chelating agents have also been applied in synthesis of battery precursors using the carbonate coprecipitation system. In 2005 in a paper from Park et al., carbonate coprecipitation was modified by the addition of $NH_3.H_2O$ as the chelating agent, and

regular spherical-shaped precipitate particles with relatively monodisperse diameters of around 10 um were obtained. The particles well-retained the secondary morphology of the precursor after high temperature calcination and annealing processes [134]. The primary aggregates that comprised the secondary structure were still relatively loose and could be broken by ultrasonication, and in the manuscript the loose structure was noted to potentially accommodate volume change during Li intercalation/deintercalation. The improved uniformity of the obtained particles was explained as resulting from the use of the chelating agent according to a similar mechanism as stated in Samsung's work [110], functioning to prevent phase separation and to facilitate the formation of homogeneous and uniform particles. Robinson et al. published a qualitative work on the particle nucleation and growth process of manganese carbonate coprecipitation in a batch reactor [51], in which NH_4HCO_3 was used as the coprecipitation agent. The transition of particle shape from cube to sphere was observed as the concentration of manganese ion was increased at different NH_4HCO_3 to manganese ratios. This transition was attributed to the different sizes of the initially formed primary particles; initial primary particles with sizes under a certain threshold would aggregate into larger spherical particles.

While many of the previous reports focused on the hypothesis that slow growth and dense hydroxide particles resulted from ammonia complexing TM and slowly releasing the complex to the hydroxide solid phase (see Equations 1 and 2), Van Bommel et al. published a study that highlighted a different process [52]. In this report, the slow growth and high tap density precipitate particles were attributed to the equilibrium between TM hydroxide particles and aqueous ammonia TM complexes in solution as shown below:

$$M(OH)_2 + nNH_3 \leftrightarrow [M(NH_3)_n]^{2+} + 2OH^- \quad (3)$$

It was found that dense spherical particles only grew in the pH range where metal ions coordinated with ammonia, and the chelation effect was speculated to result in a dynamic dissolution-recrystallization of the hydroxide that resulted in lower particle internal porosity and higher tap density. The authors suggested that both the

release of the complexed ammonia to the hydroxide and the dissolution-recrystallization was occurring during the coprecipitation reaction [51] . It was also suggested that the binding strength between the chelating agent and the precipitate particles could impact the resulting particle morphologies.

It is noted briefly that while ammonia is the most common chelation agent used in coprecipitation synthesis of battery precursor particles, others have also been explored. For example, Zhang et al. used poly(ethylene glycol) (PEG) to facilitate oxalate coprecipitation [126]. Oxalate itself forms complexes with TMs commonly used in battery precursor coprecipitation and thus can serve a similar function to a chelation agent at relatively low TM concentrations [83].

4.3. pH

The influence of pH in hydroxide precipitation is dramatic because it not only impacts the chemistry and complexes of the different species that form in solution but also hydroxide ion is the target precipitation agent and thus higher pH means greater driving force for nucleation and growth. In agreement to the normal rule that higher supersaturation and faster precipitation speed results in smaller particles, it has been reported in hydroxide coprecipitation that the average particle size decreased with increasing pH [127,135]. Particle morphology changes at different pH values has been reported in multiple studies. The dependence of particle morphology on solution pH was systematically investigated by Bommel et al. in 2009 [52]. As shown in Figure 4, spherical particles with smooth surfaces can be obtained from synthesis at pH values of 11.4 or less, which will be able to more uniformly and densely grow and thus produce higher tap density for the materials compared to the irregular shaped particles. Through tracking the particle morphology and tap density, and conducting equilibrium calculations of the coprecipitation solution, the pH range where all the appropriate TM ions coordinated with ammonia was targeted to facilitate the growth of regular-shaped spherical particles with high tap density. pH effects are not restricted to hydroxide - Wang et al. reported that oxalate particles transformed from cubic to lamellar morphology as pH was increased from 1 to 7 with ammonia

chelating agent present in the solution [121]. More detailed discussion on particle morphology will be covered below in Section 5.

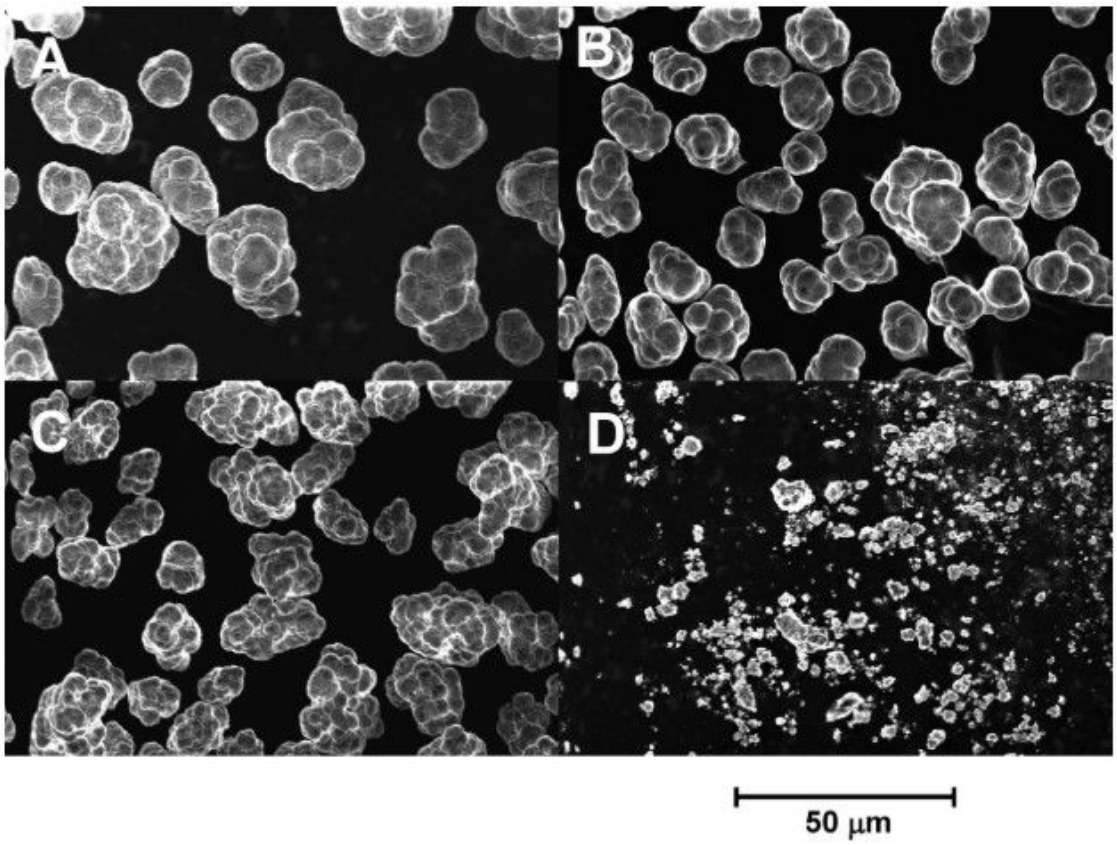

Figure 4 SEM images of $Ni(OH)_2$ particles synthesized from coprecipitation reactions with a pH value of A) 10.6, B) 11.0, C) 11.4, and D) 11.8 while other solution conditions were controlled the same in a continuous system. Reprinted with permission from [52]. Copyright (2009) American Chemical Society.

5. Fundamental solution chemistry and nucleation and growth studies

Fundamental studies of coprecipitation solution chemistry, the complexes that form, and nucleation and particle growth processes is important to understand and predict the resulting precipitate composition and morphology. Often the target is dense spherical particles to obtain high tap density and electrode loading, but many other morphologies have been reported to have desirable electrochemical performance [24,51,136,137]. In addition, explicit compositional control is needed both to achieve target

compositions with high accuracy and reproducibility and to obtain more complex particles that have variation in composition within the particles.

5.1. Solution equilibrium

Van Bommel et al. previously reported the use of equilibrium calculations to study the effect of pH on particle morphologies in a mixed TM hydroxide reaction system with ammonia as the chelating agent [52]. By using the system of equations that included equilibrium constants and mole balances, they predicted the concentration of metal-ammonia complexes for both pure and mixed TM systems. The experimentally obtained tap densities from particles synthesized at different pH were then evaluated in the context of the extent of complexation of the TM species as a function of solution pH. Spherical dense hydroxide is produced in the pH range where ammonia complexation was calculated to be significant – while at high pH values where little complexation was calculated the resulting particles were small, irregular, and had low tap density. This study was one of the first few that integrated solution chemistry calculations with predictions on the final physical properties or morphologies of the resulting precipitate particles. In 2011, Wang et al. used equilibrium calculations on a carbonate coprecipitation process in a blend solution of Mn and Ni to guide the selection of solution conditions [117]. The residual TM concentration in the solution was calculated as a function of pH and it was determined that the pH range of 7.5 to 8.5 would minimize the residual TM concentration that did not precipitate to the solid phase. Lower pH was predicted to inhibit complete carbonate precipitation reaction while higher pH would increase the residual TM due to the formation of ammonia complexes, and even higher pH would result in hydroxide coprecipitation.

In 2015, Robinson et al. published a work on the tunability of particle morphology in manganese carbonate coprecipitation [51], in which equilibrium calculations were used to determine the amount of ammonia complex formation in the solution at different NH_4HCO_3 to Mn^{2+} ratios. It should be noted that NH_4HCO_3 could function both as the coprecipitation agent and as the chelating agent – with NH_4^+ in the salt providing the

source for the complexing NH_3 and CO_3^{2-} serving as the coprecipitation anion. Equilibrium calculations determined that less than 0.1% of the feed Mn remained in the solution as a soluble complex at equilibrium across a wide range of solution conditions, and that the residual manganese concentration decreased as the relative or absolute NH_4HCO_3 amount increased. This outcome was largely due to the relatively neutral pH of the solution, which resulted in NH_4^+ being the dominant species in the ammonia/ammonium equilibrium and thus relatively small amounts of NH_3 were available to form $Mn(NH_3)_n^{2+}$ complexes. Although the NH_3 complexation was low as determined by equilibrium calculations, substitution of NH_4HCO_3 with $NaHCO_3$ as the coprecipitation agent changed the particle morphology from cubic to spherical suggesting that even small amounts of complexation of TM may have significant impacts on initial particle nucleation.

Wang et al. applied equilibrium calculations to oxalate coprecipitation in a solution containing both Mn and Ni [121]. Oxalic acid was used as the coprecipitation reagent and either ammonia or hydroxide was used to control the solution pH. Both equilibrium calculations and experiments revealed that there was an optimal pH range to maximize the conversion of the TM cations to the solid phase precipitates. Calculations indicated that the residual Mn in the solution phase was four times that of the residual Ni at all pH values due to differences in solubility, which resulted in the Mn:Ni ratio in the obtained precipitates lower than the feed ratio. These composition deviations were not compensated by the addition of ammonia even though ammonia coordinates more Ni than Mn.

5.2. Coprecipitation kinetics

Understanding the kinetics of the nucleation and particle growth for both single and multicomponent TM solutions is also critical for rational and explicit control of particle composition and morphology. Some reports have developed models to describe the reaction, nucleation, and particle growth process of the coprecipitation system [138,139]; however, coprecipitation is a complex process where conditions such as pH, concentration, temperature, complexing agents, morphology-directing agents,

and stir rate can all significantly impact final particle yield, composition, and morphology. Changes to the reagent feeding rates, the composition of the reactants and product particles, smoothness of the reactor surface and the abovementioned factors may direct the nucleation towards a different path (homogeneous nucleation or heterogeneous nucleation) or the particle growth towards different driving forces (diffusion controlled or surface controlled). This complexity likely underlies why there have been very few studies which develop a model in the coprecipitation synthesis for battery materials, because developing a broadly applicable model to many experimental conditions would be challenging [117]. Even experimental studies aimed at gaining kinetic information are generally qualitative or semi-quantitative. In part this is due to the disparate length (from nanometers initial or pre-nuclei to submicron primary particles to tens of micrometers secondary particles) and time (from the rare event and fractions of a second initial nucleation to the many hours precipitation process; or possibly longer for continuous reactor operations) scales.

Van Bommel et al. tracked the tap density and particle morphology of $Ni(OH)_2$ particles as a function of time in a CSTR coprecipitation reactor [52]. It was found that the tap density of the particles gradually increased and then plateaued after ~10 hours at ~2 g cm^{-3}. The gradual formation of spherical particles which became larger and smoother over the first 10 hours of the process, as revealed with SEM (shown in Figure 5), was given as the explanation for the tap density observations. Wang et al. also used SEMs from particles at different reaction times in a carbonate coprecipitation study [117], and similarly it was found that the formation of dense, smooth, spherical particles took ~8 hours. Particles collected <1 hour after initiation of the reaction were particularly irregular with wide size distributions of the secondary particles from 1 to 80 μm. Within the limits of the reaction time in this study in a CSTR, it was also found that the secondary particles continued to increase in diameter for the entirety of the process. These studies provided valuable insights into the coprecipitation timescale to achieve dense and spherical particles with both hydroxide and carbonate processes, although the systems were limited to a specific

subset of experimental conditions. Note that in both studies the CSTR starts with a TM concentration (of both feed or soluble species and precipitates) within the reactor of zero and thus part of the increase in particle size and tap density is the reactor reaching steady state with regards to concentration of total TM and coprecipitation anion.

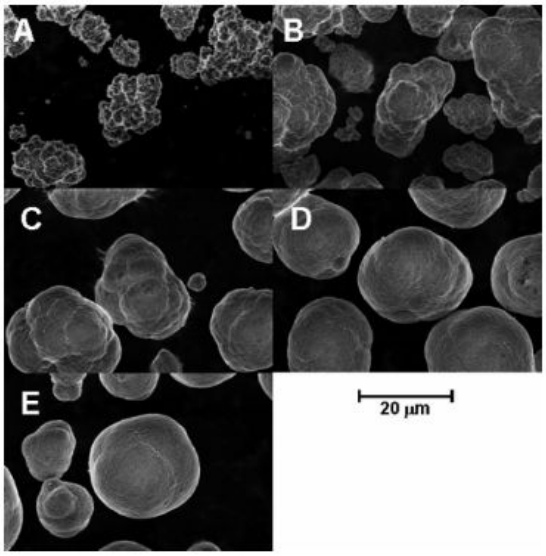

Figure 5 SEM images of $Ni(OH)_2$ harvested from the same coprecipitation reactions after A) 2 hours, B) 5 hours, C) 10 hours, D) 15 hours , and E) 20 hours. Reprinted with permission from [52]. Copyright (2009) American Chemical Society.

Dong et al. tracked the rate of coprecipitation of Ni and Mn oxalate in solutions containing only a single TM and a blend of the TMs in batch reactors [22]. It was found that the pure Mn and Ni oxalate particles precipitated at very different rates, but that in the blend system Mn and Ni precipitate at nearly identical rates. This outcome was rationalized by postulating that faster-nucleating Mn oxalate particles functioned as seeds to facilitate faster Ni precipitation. This report demonstrated that even though TMs can have very different solubilities and precipitation rates, under certain conditions and timescales the resulting precipitate particles can have compositions that match the feed stoichiometry due to synergistic interactions with regards to the nucleation and growth rates and the most favorable precipitate structure. In a follow up study, Dong et al. used the focused beam reflectance measurement technique to in-situ track the particle size distribution (PSD) as a function of reaction time in the

oxalate coprecipitation system with the same TM feed compositions as before (pure Mn, pure Ni, and Mn/Ni blend feed), two example results being shown in Figure 6. The initial nucleated particles from the solution were detected with the sharp peak with narrow size distribution, followed by gradual increase of particle size and expansion of the PSD. Different coprecipitation reactions will result in different PSD evolution patterns, which can be used to understand the crystallization mechanism. The combination of in-situ compositional information and PSDs provided quantitative details of reaction rate, reaction order, and insights into the mechanisms of particle nucleation and growth [140]. Further work is still needed to provide a more complete understanding of the process and to enable precise design and control of particle PSD. Note that the kinetic studies were conducted in batch reactors which have a continuously decreasing ion concentration during the reaction process that results in the particle growth process becoming supply-controlled.

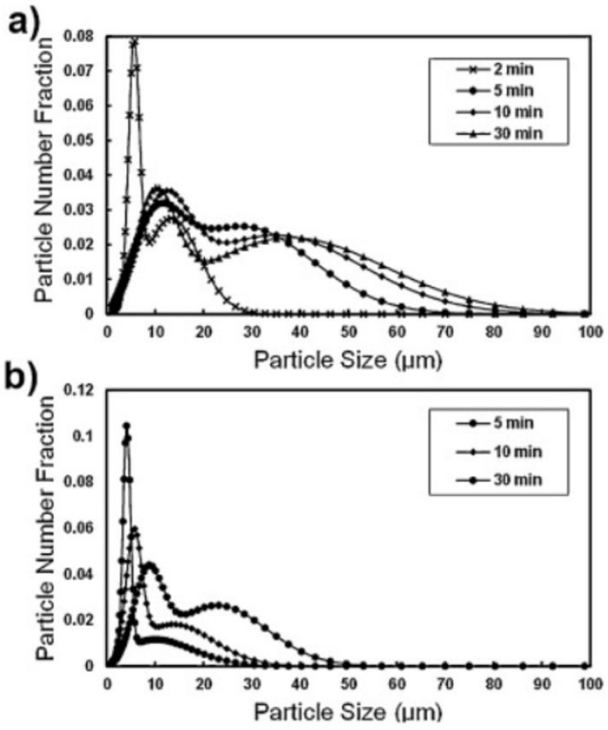

Figure 6 Particle size distributions at 5, 10, and 30 min after the start of the precipitation in a) manganese oxalate, b) nickel oxalate coprecipitations. Solid lines added to guide the eye. Reprinted with permission from [140]. Copyright (2018) Elsevier.

6. Additional Particle Complexity

Many promising cathode materials with high energy density, in particular Ni-rich layered oxides, have tradeoffs of less stability in the oxidized/charged state and lower temperatures of thermal decomposition compared to other TM oxides [34,141]. High valence Ni ions have been associated with the issues of electrolyte oxidation, oxygen release from the oxide structure, and phase change to electrochemically inactive structures. Sun et al. proposed and reported on the synthesis of particles via coprecipitation where there was a core enriched in Ni and a shell with a lower Ni composition to take advantage of a core with high energy density and a shell that provided stability particularly to the contacting electrolyte phase to reduce electrolyte decomposition and improve thermal stability of the cathode material [34]. The target composition for the inner core was $Li[Ni_{0.8}Co_{0.1}Mn_{0.1}]O_2$ and the outer shell was $Li[Ni_{0.5}Mn_{0.5}]O_2$. The initial specific capacity of the core-shell cathodes was a little bit less than the pure core materials; however, the capacity retention after 500 cycles was 98% for the core-shell cathodes, much higher than the 81% of the pure core material. Differential scanning calorimetry measured higher onset temperature for the core-shell structure also with less heat release, suggesting improvements in thermal stability and safety. The core-shell material properties were also compared to the mechanical mixture of core and shell materials of equivalent fractions (as separate particles as opposed to integrated as core-shell particles) in a later report, and the core-shell still had better cycling and thermal stability – demonstrating the importance in achieving the more complex compositional profile in the active material [142]. The encouraging properties of core-shell particles resulted in multiple follow up reports of variations in the particle structure and/or composition [141,143–146]. The core-shell structure was revealed using SEM cross-section images, and the composition transition within the particle was also experimentally probed and validated [34,141,147].

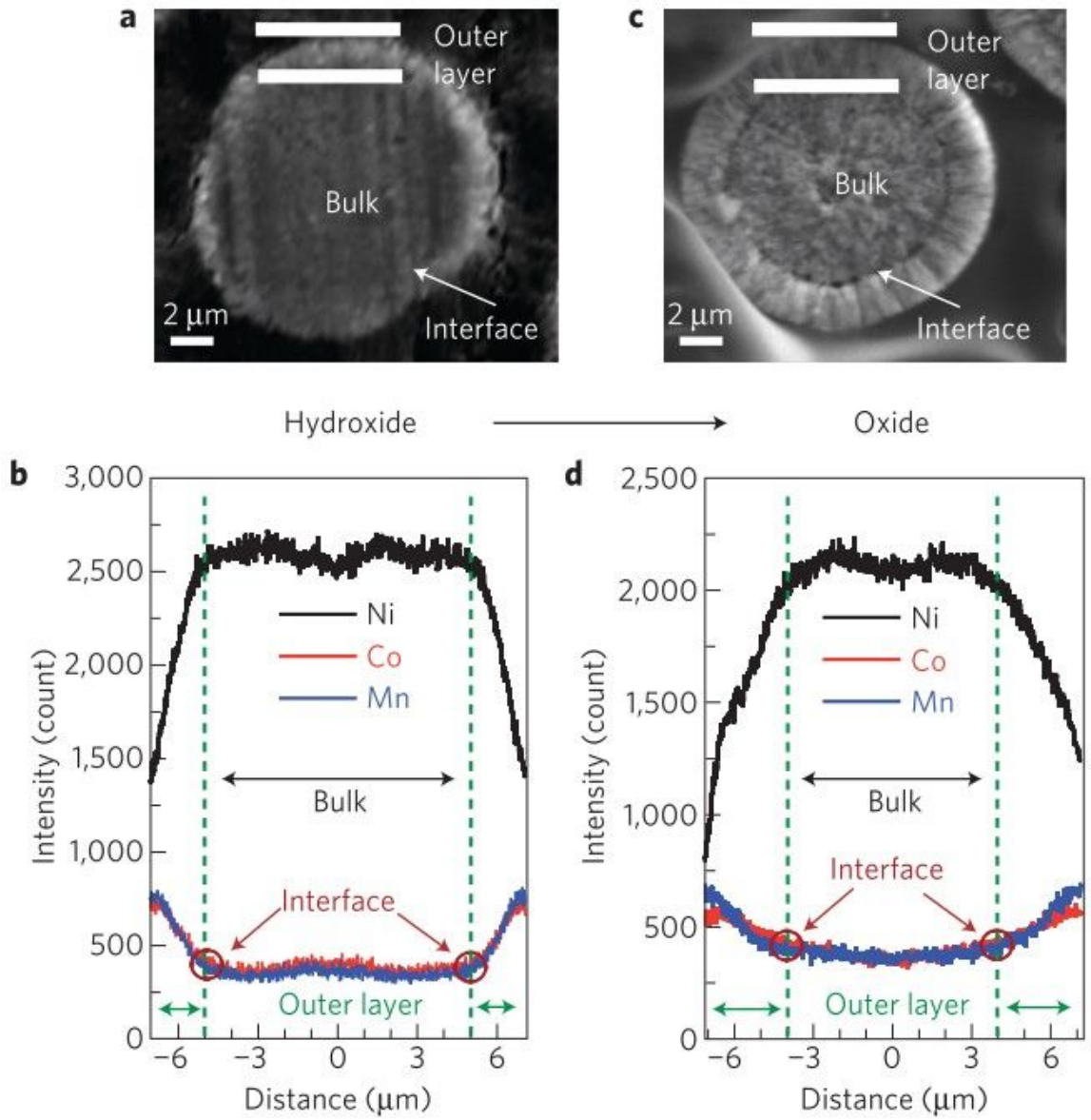

Figure 7 Scanning electron microscopy (SEM) image (a) and electron-probe X-ray micro-analysis (EPMA) line scan results (b) of precursor hydroxide; SEM image (c) and EPMA line scan (d) of the final lithiated oxide $Li[Ni_{0.64}Co_{0.18}Mn_{0.18}]O_2$. In both cases, the gradual concentration changes of Ni, Mn, and Co in the interlayer are clearly evident. The Ni concentration decreases and the Co and Mn concentrations increase towards the surface. Reprinted with permission from [2].

Compared to other synthesis techniques to apply a protective coating to particle surfaces, such as sol-gel coating [148], chemical vapor deposition (CVD) [149,150], or atomic layer deposition (ALD) [151,152], shells deposited on coprecipitation precursors are relatively thick (often µm-scale) and can be integrated with the production process of the core active material, often not requiring an additional processing step or

additional equipment. Since a following calcination process is needed to convert the core-shell precursor into the final core-shell active materials, the calcination profile and duration need to be carefully chosen to avoid excessive inter-diffusion of the TMs, which at an extreme case would result in a single composition particle with an average composition of a blend of the core and shell. Generating core-shell microstructures via coprecipitation is challenging, and maintaining these microstructures after sintering can be even more challenging. Efforts to understand and/or control the interdiffusion of ions between core and shell during calcination have been reported [34,147,153,154]. Mild inter-diffusion can be beneficial for spreading out the interfacial region between the core and shell and mitigating voids or separation that can occur during calcination and/or cycling due to the different volumetric change between the distinct core and shell composition materials [2]. Dahn et al. have also conducted a study to measure the interdiffusion rates of different transition metal ion couples during calcination process which can be used to predictably synthesize final oxide materials core and shell compositional profiles [155].

To further mitigate voids between the core and shell regions that can result due to their different volume change during processing and/or cycling, a modification to the synthesis was reported where a shell with a gradient in composition was precipitated onto single composition core particles [2]. As shown in Figure 7, Sun et al. synthesized a core of $Li[Ni_{0.8}Co_{0.1}Mn_{0.1}]O_2$ and a shell which gradually went from the same composition as the core to $Li[Ni_{0.46}Co_{0.23}Mn_{0.31}]O_2$ at the surface over a length scale of 3 μm, gradually increasing in Mn and decreasing in Ni. The gradient was obtained by careful control of the composition of the TM feed to the coprecipitation reactor. Initial discharge capacity of the concentration-gradient material was only slightly less than the nickel rich core, whereas the capacity retention after 50 cycles at 55 °C was 96%, much higher than the 67% of the core material alone. Room temperature comparison of 500 cycles showed 96.5% retention for the concentration-gradient material compared to 80.4% for the core particles. Careful inspection of cross-sections of the core-concentration gradient shell particles (Figure 7) revealed that the particles did not have as distinct or separated of interface or void regions associated with previous

core-shell particles, and follow-on studies demonstrated even better integration of the core and shell to mitigate void formation and stress in the interface region [119,156–160].

In the core-shell and core-gradient shell examples above the solution chemistry was all hydroxide precipitation and the target materials after calcination were layered metal oxides. Coprecipitation of particles with other structures, chemistry, and compositional profiles have also been demonstrated. For example, carbonate coprecipitation was used to produce particles with a gradient initiated at the start of synthesis as opposed to only for the shell region, and the target was Li-and Mn-enriched high capacity cathode final materials with an overall much higher Mn fraction [119]. Coprecipitation of compositionally varying particles has also been applied to produce phosphate final materials, where the high capacity $LiMn_{0.85}Fe_{0.15}PO_4$ olivine core was combined with a $LiFePO_4$ surface with the goal to improve the conductivity of the final material [35]. Full concentration-gradient layered cathode has also been applied to produce layered-phase final materials where the nickel concentration decreases linearly as the manganese concentration increases from the center to the surface of the particle [159]. Hou et al. recently published a review paper focused on core-shell and concentration-gradient particles prepared via coprecipitation which details other reports in the literature [161].

7. Future directions

As more knowledge and insights are gained about the relationship between reaction conditions and coprecipitated product particle properties, computational models will be developed to guide the choice of reaction conditions to synthesize target product particles with explicit compositions and morphologies. Such models will need to account for a wide range of reaction parameters, and to provide an accurate prediction of all the physical and chemical processes during the coprecipitation reaction. A recently published paper by Barai et al. reported progress in predicting precursor particle properties from hydroxide coprecipitation. The computational

outcomes were comparable on some metrics to the experimental results, but some particle properties such as particle shape and size distribution were difficult to capture with the model [162]. Further advances in the development of such models, coupled with deeper understanding of the coprecipitation processes, are expected to result in predictions of higher resolution and to guide the control of reaction conditions and chemical selection.

Meanwhile it is expected that the design space is expected to expand as the kinetics of coprecipitation becomes better understood. Although there have been a diversity of particle morphologies reported for coprecipitation, compared to other synthesis routes such as hydrothermal there are many more morphologies that could be achieved. Hydrothermal synthesis, however, requires the higher temperatures and longer reaction times relative to coprecipitation to obtain target particles. Coprecipitation could in principle achieve similar diversity of particle morphology to hydrothermal synthesis with more mild synthesis conditions if greater knowledge is gained in the nucleation and growth processes and appropriate structure directing agents are implemented.

To pursue fundamental knowledge of the coprecipitation process, advanced characterization methods will be needed. Tools with the ability to in-situ measure the solution concentrations and particle morphologies, as well as characterization methods to investigate the cation and phase distribution within the precipitated particles, are critical for gaining reliable information of the reaction process and particles obtained, so that correlation between reaction process and particle product can be achieved. Thus far, the battery materials synthesis field has devoted many complex materials characterization tools and great effort to study the materials properties and chemistry of final active materials, but much less effort has been applied to understand precursor particles. This is not surprising given that the final active materials are used in the electrochemical device, however, for final materials produced using precursors, the properties of the precursor in many cases dictates the final properties of the active material. More emphasis should be put into the study of

coprecipitation reaction and the precursors, including the processes of precursor formation, the processes of precursor decomposition and conversion to final material, and the detailed structure and composition of the resulting precursor particles.

Conclusion

Coprecipitation is a popular method for the synthesis of precursors used in the production of Li-ion battery materials. While the reaction is straightforward and easy to conduct in the lab, careful control over the reaction conditions is essential for the synthesis of particles with controllable, reproducible, and monodisperse particle size and shape. Prediction of the resulting particle morphology and composition requires fundamental knowledge of the coprecipitation process. In this paper, the considerations for each of the most common types of coprecipitation crystallizations used for synthesis of Li-ion battery materials were reviewed - hydroxide, carbonate, and oxalate. Depending on the cations involved in the reaction and different objectives in terms of synthesis simplicity and particle properties, one type of process often will be preferred. Key process conditions and their influence on the properties of the resulting crystalline particles were also reviewed with highlight examples from recent reports. In the field of battery materials synthesis, where tap density of particle powders is often a priority, monodisperse spherical particles are often targeted, which generally require high stirring rate, the use of a chelating agent, and careful selection of pH solution concentrations of reagents. Inclusion of coprecipitation to synthesize core-shell and concentration gradient particles was described in this review to demonstrate the versatile capability of coprecipitation for the synthesis of particles with complex composition and structure. Some recent advances in understanding the equilibrium and kinetics of coprecipitation reactions were also summarized, with an emphasis of the methods and tools being developed, which ideally will motivate further research into the fundamental processes in this complex reaction system towards precise and predictable control over the crystalline precursor particle synthesis.

Acknowledgements

This work was funded by the National Science Foundation, through grant award CBET-1652488. The authors also thank Ningning Song for her help in drawing the table of contents graph.

References

1 J. B. Goodenough and Y. Kim, *Chem. Mater.*, 2010, **22**, 587–603.

2 Y. K. Sun, S. T. Myung, B. C. Park, J. Prakash, I. Belharouak and K. Amine, *Nat. Mater.*, 2009, **8**, 320–324.

3 M. Hu, X. Pang and Z. Zhou, *J. Power Sources*, 2013, **237**, 229–242.

4 E. Vinodkumar, R. Marom, R. Elazari, G. Salitra and D. Aurbach, *Energy Environ. Sci.*, 2011, **4**, 3243–3262.

5 R. Marom, S. F. Amalraj, N. Leifer, D. Jacob and D. Aurbach, *J. Mater. Chem.*, 2011, **21**, 9938–9954.

6 R. Van Noorden, *Nature*, 2014, **507**, 26–28.

7 T. Ohzuku, A. Ueda, M. Nagayama, Y. Iwakoshi and H. Komori, *Electrochim. Acta*, 1993, **38**, 1159–1167.

8 J. M. Tarascon, *J. Electrochem. Soc.*, 1991, **138**, 2859.

9 R. J. Gummow and M. M. Thackeray, *Solid State Ionics*, 1992, **53–56**, 681–687.

10 Q. Zhong, A. Bonakclarpour, M. Zhang, Y. Gao and J. R. Dahn, *J Electrochem Soc*, 1997, **144**, 205–213.

11 D. Guan, C. Cai and Y. Wang, *2011 IEEE Green Technol. Conf. Green 2011*, 2011, 1465–1469.

12 F. Wu, Z. Wang, Y. Su, Y. Guan, Y. Jin, N. Yan, J. Tian, L. Bao and S. Chen, *J. Power Sources*, 2014, **267**, 337–346.

13 S.-M. Park, T.-H. Cho and M. Yoshio, *Chem. Lett.*, 2004, **33**, 748–749.

14 L. Li, S. Song, X. Zhang, R. Chen, J. Lu, F. Wu and K. Amine, *J. Power Sources*, 2014, **272**, 922–928.

15 G. M. Koenig, I. Belharouak, H. M. Wu and K. Amine, *Electrochim. Acta*, 2011,

56, 1426–1431.

16 I. Belharouak, G. M. Koenig and K. Amine, *J. Power Sources*, 2011, **196**, 10344–10350.

17 C. J. Bae, C. K. Erdonmez, J. W. Halloran and Y. M. Chiang, *Adv. Mater.*, 2013, **25**, 1254–1258.

18 H. Dong and G. M. Koenig, *J. Mater. Chem. A*, , DOI:10.1039/c7ta03653a.

19 C. Tan, H. Luo, K. Du, D. Huang and K. Hu, 2018, **6**, 1293–1304.

20 M. Ebner, D. W. Chung, R. E. García and V. Wood, *Adv. Energy Mater.*, 2014, **4**, 1–6.

21 J. Billaud, F. Bouville, T. Magrini, C. Villevieille and A. R. Studart, *Nat. Energy*, 2016, **1**, 1–13.

22 H. Dong and G. M. Koenig Jr, *J. Mater. Chem. A*, 2017, **5**, 13785–13798.

23 R. Thirunakaran, G. H. Lew and W. S. Yoon, *Powder Technol.*, 2016, **301**, 197–210.

24 L. Zhang, W. Borong, L. Ning and W. Feng, *Electrochim. Acta*, 2014, **118**, 67–74.

25 H. Li, Q. Xu, X.-X. Shi, D.-W. Song and L.-Q. Zhang, *Rare Met.*, 2015, **34**, 580–585.

26 H. Dong, A. Wang and G. M. Koenig, *Powder Technol.*, , DOI:10.1016/j.powtec.2018.05.020.

27 M. a. Valenzuela, P. Bosch, G. Aguilar-Rios, a. Montoya and I. Schifter, *J. Sol-Gel Sci. Technol.*, 1997, **8**, 107–110.

28 D. Wang, I. Belharouak, G. M. Koenig, G. Zhou and K. Amine, *J. Mater. Chem.*, 2011, **21**, 9290.

29 J.-H. Ju and K.-S. Ryu, *J. Alloys Compd.*, 2011, **509**, 7985–7992.

30 Y. Fan, J. Wang, X. Ye and J. Zhang, *Mater. Chem. Phys.*, 2007, **103**, 19–23.

31 Y. U. Park, J. Kim, H. Gwon, D. H. Seo, S. W. Kim and K. Kang, *Chem. Mater.*, 2010, **22**, 2573–2581.

32 Y. Kim and D. Kim, *ACS Appl. Mater. Interfaces*, 2012, **4**, 586–589.

33 T. H. H. Cho, S. M. M. Park, M. Yoshio, T. Hirai and Y. Hideshima, *J. Power Sources*, 2005, **142**, 306–312.

34 Y. K. Sun, S. T. Myung, M. H. Kim, J. Prakash and K. Amine, *J. Am. Chem. Soc.*,

2005, **127**, 13411–13418.

35 S. M. Oh, S. T. Myung, J. B. Park, B. Scrosati, K. Amine and Y. K. Sun, *Angew. Chemie - Int. Ed.*, 2012, **51**, 1853–1856.

36 D. Wang, I. Belharouak, L. H. Ortega, X. Zhang, R. Xu, D. Zhou, G. Zhou and K. Amine, *J. Power Sources*, 2015, **274**, 451–457.

37 M. H. Kim, H. S. Shin, D. Shin and Y. K. Sun, *J. Power Sources*, 2006, **159**, 1328–1333.

38 S.-M. Oh, S.-T. Myung, Y. S. Choi, K. H. Oh and Y.-K. Sun, *J. Mater. Chem.*, 2011, **21**, 19368.

39 D.-K. Lee, S.-H. Park, K. Amine, H. J. Bang, J. Parakash and Y.-K. Sun, *J. Power Sources*, 2006, **162**, 1346–1350.

40 J.-H. Lim, H. Bang, K.-S. Lee, K. Amine and Y.-K. Sun, *J. Power Sources*, 2009, **189**, 571–575.

41 H. B. Lin, J. N. Hu, H. B. Rong, Y. M. Zhang, S. W. Mai, L. D. Xing, M. Q. Xu, X. P. Li and W. S. Li, *J. Mater. Chem. A*, 2014, **2**, 9272–9279.

42 N. Wu, H. Wu, W. Yuan, S. Liu, J. Liao and Y. Zhang, *J. Mater. Chem. A*, 2015, **3**, 13648–13652.

43 C. Zhao, X. Wang, R. Liu, F. Xu and Q. Shen, *RSC Adv.*, 2014, **4**, 7154–7159.

44 L. Yi, Y. Wang, B. Wu, R. Yu, Z. Liu, M. Liu, X. Wang, X. Yang, X. Zhang, G. Wang, X. Xiong and M. Liu, *ACS Appl. Mater. Interfaces*, 2017, **9**, 25358–25368.

45 B.-J. Hwang, K.-F. Hsu, S.-K. Hu, M.-Y. Cheng, T.-C. Chou, S.-Y. Tsay and R. Santhanam, *J. Power Sources*, 2009, **194**, 515–519.

46 S. Li, G. Ma, B. Guo, Z. Yang, X. Fan, Z. Chen and W. Zhang, *Ind. Eng. Chem. Res.*, 2016, **55**, 9352–9361.

47 C.-L. Xu, W. Xiang, Z.-G. Wu, Y.-D. Xu, Y.-C. Li, H.-T. Li, Y. Xiao, B.-C. Tan, X.-D. Guo and B.-H. Zhong, *J. Alloys Compd.*, 2019, **777**, 434–442.

48 G. Ma, S. Li, W. Zhang, Z. Yang, S. Liu, X. Fan, F. Chen, Y. Tian, W. Zhang, S. Yang and M. Li, *Angew. Chemie - Int. Ed.*, 2016, 3667–3671.

49 S. Huang, H. Wu, P. Chen, Y. Guo, B. Nie, B. Chen, H. Liu and Y. Zhang, *J. Mater. Chem. A*, 2015, **3**, 3633–3640.

50 S. Zhang, C. Deng, B. L. Fu, S. Y. Yang and L. Ma, *Powder Technol.*, 2010, **198**,

373–380.

51 J. P. Robinson and G. M. Koenig, *Powder Technol.*, 2015, **284**, 225–230.

52 A. Van Bomme and J. R. Dahn, *Chem. Mater.*, 2009, **21**, 1500–1503.

53 S. Jouanneau, K. W. Eberman, L. J. Krause and J. R. Dahn, *J. Electrochem. Soc.*, 2003, **150**, A1637.

54 W. Song, P. Shen, H. Ma, J. Chen, J. Zhao, F. Cheng and C. Li, *Inorg. Chem.*, 2006, **45**, 2038–2044.

55 M. A. McCaffrey, B. Lazar and H. D. Holland, *J. Sediment. Res.*, 1987, **57**, 928–937.

56 A. I. Petrov, D. V. Volodkin and G. B. Sukhorukov, *Biotechnol. Prog.*, 2005, **21**, 918–925.

57 M. Haruta, N. Yamada, T. Kobayashi and S. Iijima, *J. Catal.*, 1989, **115**, 301–309.

58 Q. Chen, A. J. Rondinone, B. C. Chakoumakos and Z. John Zhang, *J. Magn. Magn. Mater.*, 1999, **194**, 1–7.

59 S. Choo, H. Y. Kim, D. Y. Yoon, W. Choi, S. H. Oh, J. B. Ju, J. M. Ko, H. Jang and W. Il Cho, *Korean J. Chem. Eng.*, 2014, **31**, 905–910.

60 R. C. Longo, F. T. Kong, S. KC, M. S. Park, J. Yoon, D. H. Yeon, J. H. Park, S. G. Doo and K. Cho, *Phys. Chem. Chem. Phys.*, 2014, **16**, 11218–11227.

61 S. Wongsaenmai, R. Yimnirun and S. Ananta, *Effects of calcination conditions on phase formation and particle size of indium niobate nanopowders synthesized by the solid-state reaction*, 2007, vol. 61.

62 S. Levasseur, M. Menetrier and C. Delmas, *Chem. Mater.*, 2002, **14**, 3584–3590.

63 K. Amine, H. Tukamoto, H. Yasuda and Y. Fujita, *J. Power Sources*, 1997, **68**, 604–608.

64 T. Dong-Ge, L. Qiong-Yu, W. Ni-Ni, T. Ai-Dong, T. Lian-Xing, H. Ke-Long and J. Xiao-Yang, *Mater. Chem. Phys.*, 2005, **94**, 423–428.

65 M. A. Mohamed, A. K. Galwey and S. A. Halawy, *Thermochim. Acta*, 2005, **429**, 57–72.

66 H. Dong, A. Wang and G. M. Koenig, *Powder Technol.*, 2018, **335**, 137–146.

67 K. Mizushima, P. C. Jones, P. J. Wiseman and J. B. Goodenough, *Mater. Res. Bull.*, 1980, **15**, 783–789.

68 A. K. Padhi, K. S. Nanjundaswamy and J. B. Goodenough, 1997, **144**, 2–8.

69 M. M. Thackeray, W. I. F. David, P. G. Bruce and J. B. Goodenough, *Mater. Res. Bull.*, 1983, **18**, 461–472.

70 J. C. Hunter, *J. Solid State Chem.*, 1981, **39**, 142–147.

71 D. Guyomard and J. M. Tarascon, *Solid State Ionics*, 1994, **69**, 222–237.

72 R. Gummow, M. Thackeray, W. David and S. Hull, *Mater. Res. Bull.*, 1992, **27**, 327–337.

73 D. Zhang, B. N. Popov and R. E. White, *J. Power Sources*, 1998, **76**, 81–90.

74 S.-W. Kim, H.-W. Lee, P. Muralidharan, D.-H. Seo, W.-S. Yoon, D. K. Kim and K. Kang, *Nano Res.*, 2011, **4**, 505–510.

75 I. J. Davidson, R. S. McMillan and J. J. Murray, *J. Power Sources*, 1995, **54**, 205–208.

76 G.-M. Song, Y.-J. Wang and Y. Zhou, *J. Power Sources*, 2004, **128**, 270–277.

77 D. Guyomard and J. M. Tarascon, *J. Electrochem. Soc.*, 1992, **139**, 937–948.

78 J. M. Tarascon, D. Guyomard and G. L. Baker, *J. Power Sources*, 1993, **44**, 689–700.

79 J. M. Tarascon and D. Guyomard, *Electrochim. Acta*, 1993, **38**, 1221–1231.

80 J. M. Tarascon, *J. Electrochem. Soc.*, 1991, **138**, 2859.

81 J. N. Reimers, E. W. Fuller, E. Rossen and J. R. Dahn, *J. Electrochem. Soc.*, 1993, **140**, 3396.

82 M.-H. Lee, Y.-J. Kang, S.-T. Myung and Y.-K. Sun, *Electrochim. Acta*, 2004, **50**, 939–948.

83 Z. Zhu, D. Zhang, H. Yan, W. Li and Qilu, *J. Mater. Chem. A*, 2013, **1**, 5492.

84 S. Yamada, M. Fujiwara and M. Kanda, *J. Power Sources*, 1995, **54**, 209–213.

85 R. J. Gummow and M. M. Thackeray, *Solid State Ionics*, 1992, **53–56**, 681–687.

86 C. Delmas and I. Saadoune, *Solid State Ionics*, 1992, **53–56**, 370–375.

87 E. Zhecheva and R. Stoyanova, *Solid State Ionics*, 1993, **66**, 143–149.

88 G. Pistoia and R. Rosati, *J. Power Sources*, 1996, **58**, 135–138.

89 X. Wang, H. Hao, J. Liu, T. Huang and A. Yu, *Electrochim. Acta*, 2011, **56**, 4065–4069.

90 H. Ren, X. Li and Z. Peng, *Electrochim. Acta*, 2011, **56**, 7088–7091.

91 D. Liu, J. Han and J. B. Goodenough, *J. Power Sources*, 2010, **195**, 2918–2923.

92 H. S. Shin, S. H. Park, Y. C. Bae and Y. K. Sun, *Solid State Ionics*, 2005, **176**, 2577–2581.

93 Y. Zhu, S. H. Choi, X. Fan, J. Shin, Z. Ma, M. R. Zachariah, J. W. Choi and C. Wang, *Adv. Energy Mater.*, 2017, **7**, 1–41.

94 D. Caurant, N. Baffier, B. Garcia and J. P. Pereira-Ramos, *Solid State Ionics*, 1996, **91**, 45–54.

95 M. E. Spahr, P. Novák, B. Schnyder, O. Haas and R. Nesperh, *J. Electrochem. Soc.*, 1998, **145**, 1113–1121.

96 J. M. Paulsen, D. Larcher and J. R. Dahn, *J. Electrochem. Soc.*, 2000, **147**, 2862–2867.

97 Z. Lu and J. R. Dahn, *J. Electrochem. Soc.*, 2001, **148**, A237.

98 Z. Lu, D. D. MacNeil and J. R. Dahn, *Electrochem. Solid-State Lett.*, 2001, **4**, A200.

99 D. D. Macneil, Z. Lu and J. R. Dahn, *J. Electrochem. Soc.*, 2002, **149**, A1332-1336.

100 K. M. Shaju, G. V. Subba Rao and B. V. R. Chowdari, *Electrochim. Acta*, 2002, **48**, 145–151.

101 N. Yabuuchi and T. Ohzuku, *J. Power Sources*, 2003, **119–121**, 171–174.

102 K. K. Cheralathan, N. Y. Kang, H. S. Park, Y. J. Lee, W. C. Choi, Y. S. Ko and Y.-K. Park, *J. Power Sources*, 2010, **195**, 1486–1494.

103 M. Ebner, F. Geldmacher, F. Marone, M. Stampanoni and V. Wood, *Adv. Energy Mater.*, 2013, **3**, 845–850.

104 M. Shao, *J. Power Sources*, 2014, **270**, 475–486.

105 S. Martinet, *Nanosci. Technol.*, 2016, 471–512.

106 L. Li, L. Wang, X. Zhang, M. Xie, F. Wu and R. Chen, *ACS Appl. Mater. Interfaces*, 2015, **7**, 21939–21947.

107 Z. Yang, J. Lu, D. Bian, W. Zhang, X. Yang, J. Xia, G. Chen, H. Gu and G. Ma, *J. Power Sources*, 2014, **272**, 144–151.

108 X. Zhang, F. Cheng, J. Yang and J. Chen, 2013, 2–5.

109 W.-H. Ryu, S.-J. Lim, W.-K. Kim and H. Kwon, *J. Power Sources*, 2014, **257**, 186–191.

110 J. Cho, *Chem. Mater.*, 2000, **12**, 3089–3094.

111 A. Van Bommel and J. R. Dahn, *Chem. Mater.*, 2009, **21**, 1500–1503.

112 Y. S. Lee, Y. K. Sun, S. Ota, T. Miyashita and M. Yoshio, *Electrochem. commun.*, 2002, **4**, 989–994.

113 T. Cho, S. Park and M. Yoshio, *Chem. Lett.*, 2004, **33**, 704–705.

114 H. Groult, T. Nakajima and N. Kumagai, *Int. J. Electrochem. Sci.*, 2014, **9**, 7712–7724.

115 S. Zhang, C. Deng, S. Y. Yang and H. Niu, *J. Alloys Compd.*, 2009, **484**, 519–523.

116 E. Zhao, M. Chen, D. Chen, X. Xiao and Z. Hu, *ACS Appl. Mater. Interfaces*, 2015, **7**, 27096–27105.

117 D. Wang, I. Belharouak, G. M. Koenig, G. Zhou and K. Amine, *J. Mater. Chem.*, 2011, **21**, 9290–9295.

118 D. Wang, I. Belharouak, S. Gallagher, G. Zhou and K. Amine, *J. Mater. Chem.*, 2012, **22**, 12039–12045.

119 G. M. Koenig, I. Belharouak, H. Deng, Y.-K. Sun and K. Amine, *Chem. Mater.*, 2011, **23**, 1954–1963.

120 S. J. Harris and P. Lu, *J. Phys. Chem. C*, 2013, **117**, 6481–6492.

121 D. Wang, I. Belharouak, G. Zhou and K. Amine, *J. Electrochem. Soc.*, 2013, **160**, A3108–A3112.

122 F. Wu, H. Lu, Y. Su, N. Li, L. Bao and S. Chen, *J. Appl. Electrochem.*, 2010, **40**, 783–789.

123 M. C. López, J. L. Tirado and C. Pérez Vicente, *J. Power Sources*, 2013, **227**, 65–71.

124 J. Vázquez, P. L. López-Alemany, P. Villares and R. Jiménez-Garay, *Mater. Lett.*, 1998, **35**, 50–57.

125 A. Huizing, H. A. M. van Hal, W. Kwestroo, C. Langereis and P. C. van Loosdregt, *Mater. Res. Bull.*, 1977, **12**, 605–611.

126 X. Zhang, F. Cheng, K. Zhang, Y. Liang, S. Yang, J. Liang and J. Chen, *RSC Adv.*, 2012, **2**, 5669.

127 J. Ying, C. Wan, C. Jiang and Y. Li, *J. Power Sources*, 2001, **99**, 78–84.

128 M. Noh and J. Cho, *J. Electrochem. Soc.* , 2013, **160**, A105–A111.

129 D.-L. Vu and J. Lee, *Korean J. Chem. Eng.*, 2015, **33**, 514–526.

130 R. Mei, X. Song, Y. Yang, Z. An and J. Zhang, *RSC Adv.*, 2014, **4**, 5746–5752.

131 S. Jouanneau and J. R. Dahn, *Chem. Mater.*, 2003, **15**, 495–499.

132 G.-H. Kim, S.-T. Myung, H. J. Bang, J. Prakash and Y.-K. Sun, *Electrochem. Solid-State Lett.*, 2004, **7**, A477.

133 2013, 1.

134 S. Park, H. Shin, S. Myung and C. S. Yoon, *Chem. Mater.*, 2005, **17**, 6–8.

135 E. D. Shchukin, A. V Pertsov, E. A. Amelina and A. S. Zelenev, *Colloid and Surface Chemistry*, Elsevier Science, 2001.

136 F. Cheng, Y. Xin, J. Chen, L. Lu, X. Zhang and H. Zhou, *J. Mater. Chem. A*, 2013, **1**, 5301.

137 W. Luo, *J. Alloys Compd.*, 2015, **636**, 24–28.

138 A. S. Moskvin and A. S. Ovchinnikov, *Phys. C Supercond. its Appl.*, 1998, **296**, 250–268.

139 R. Zauner and A. G. Jones, *Chem. Eng. Sci.*, 2000, **55**, 4219–4232.

140 H. Dong, A. Wang, G. Smart, D. Johnson and G. M. Koenig, *Colloids Surfaces A Physicochem. Eng. Asp.*, 2018, **558**, 8–15.

141 P. Hou, H. Zhang, X. Deng, X. Xu and L. Zhang, *ACS Appl. Mater. Interfaces*, 2017, **9**, 29643–29653.

142 B.-C. Park, H. J. Bang, K. Amine, E. Jung and Y.-K. Sun, *J. Power Sources*, 2007, **174**, 658–662.

143 P. Hou, J. Guo, D. Song, J. Zhang, E. Zhou and L. Zhang, *Chem. Lett.*, 2012, **41**, 1712–1714.

144 G. Li, L. Qi, P. Xiao, Y. Yu, X. Chen and W. Yang, *Electrochim. Acta*, 2018, **270**, 319–329.

145 J. Duan, P. Dong, D. Wang, X. Li, Z. Xiao, Y. Zhang and G. Hu, *J. Alloys Compd.*, 2018, **739**, 335–344.

146 S. J. Yoon, S. T. Myung, H. J. Noh, J. Lu, K. Amine and Y. K. Sun, *ChemSusChem*, 2014, **7**, 3295–3303.

147 Y. Sun, S. Myung, H. Shin and Y. C. Bae, *J. Phys. Chem. B*, 2006, **110**, 6810–6815.

148 S. Liu, J. Xu, D. Li, Y. Hu, X. Liu and K. Xie, *J. Power Sources*, 2013, **232**, 258–263.

149 C. Y. Wu, G. S. Cao, H. M. Yu, J. Xie and X. B. Zhao, *J. Phys. Chem. C*, 2011, **115**, 23090–23095.

150 R. Tian, H. Liu, Y. Jiang, J. Chen, X. Tan, G. Liu, L. Zhang, X. Gu, Y. Guo, H. Wang, L. Sun and W. Chu, *ACS Appl. Mater. Interfaces*, 2015, **7**, 11377–11386.

151 X. Meng, X.-Q. Yang and X. Sun, *Adv. Mater.*, 2012, **24**, 3589–3615.

152 B. Ahmed, C. Xia and H. N. Alshareef, *Nano Today*, 2016, **11**, 250–271.

153 J. Camardese, J. Li, D. W. Abarbanel, A. T. B. Wright and J. R. Dahn, *J. Electrochem. Soc.*, 2014, **162**, A269–A277.

154 Y. K. Sun, D. H. Kim, C. S. Yoon, S. T. Myung, J. Prakash and K. Amine, *Adv. Funct. Mater.*, 2010, **20**, 485–491.

155 J. Li, R. Doig, J. Camardese, K. Plucknett and J. R. Dahn, *Chem. Mater.*, 2015, **27**, 7765–7773.

156 K. Du, C. Hua, C. Tan, Z. Peng, Y. Cao and G. Hu, *J. Power Sources*, 2014, **263**, 203–208.

157 W. Chen, Y. Li, J. Zhao, F. Yang, J. Zhang, Q. Shi and L. Mi, *RSC Adv.*, 2016, **6**, 58173–58181.

158 Y.-K. Sun, D.-H. Kim, H.-G. Jung, S.-T. Myung and K. Amine, *Electrochim. Acta*, 2010, **55**, 8621–8627.

159 Y.-K. Sun, Z. Chen, H.-J. Noh, D.-J. Lee, H.-G. Jung, Y. Ren, S. Wang, C. S. Yoon, S.-T. Myung and K. Amine, *Nat. Mater.*, 2012, **11**, 942–947.

160 Y. K. Sun, B. R. Lee, H. J. Noh, H. Wu, S. T. Myung and K. Amine, *J. Mater. Chem.*, 2011, **21**, 10108–10112.

161 P. Hou, H. Zhang, Z. Zi, L. Zhang and X. Xu, *J. Mater. Chem. A*, 2017, **5**, 4254–4279.

162 P. Barai, Z. Feng, H. Kondo and V. Srinivasan, *J. Phys. Chem. B*, 2019, **123**, 3291–3303.

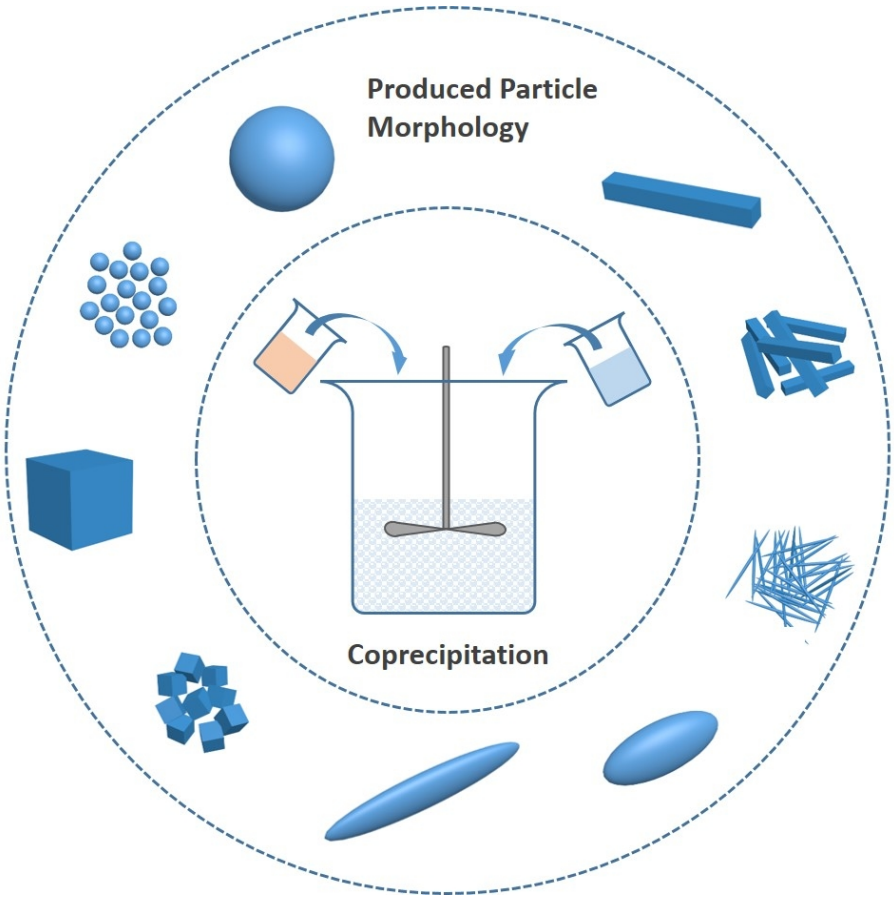

177x157mm (150 x 150 DPI)